Adaptive Control of a Master-Slave System for Teleoperated Needle Insertion under MRI-Guidance

E. Franco, M. Ristic, *Members, IEEE*

***Abstract*— This paper presents the control of a master-slave system for teleoperated needle insertion under guidance by Magnetic Resonance Imaging (MRI). The primary aim of our research is the robot-assisted laser ablation of liver tumors. The master-slave system consists of a master unit that sits next to the operator, outside the scanner room, and of a slave unit located inside the cylindrical MRI scanner. The needle insertion force is measured with a specially designed fiber optic force sensor mounted on the slave unit. Pneumatic actuation is employed in both master and slave in order to minimize the interference with the MRI environment. Accurate position control of the slave unit is achieved with a Time Delay Control scheme (TDC). Differently from previous designs, the force feedback on the master unit is provided by an adaptive controller that compensates the friction of the pneumatic actuator. The advantages over a baseline force controller are demonstrated with experiments on silicone rubber phantoms.**

***Index Terms*: Medical Robotics, Teleoperation, Immersion and Invariance, Pneumatic Systems.**

I. Introduction

MRI-guided percutaneous interventions offer better targeting accuracy compared to ultrasound guidance or computed tomography however the access to the patient in the scanner bore is limited. Recently, robotic devices have been successfully employed in order to overcome this limitation. In particular, master-slave systems have been proposed for teleoperated needle insertion [1]-[6]. Due to the constraints imposed by the strong magnetic field, the choice of actuators and sensors is however restricted [7]. Ultrasonic and piezoelectric motors have been typically employed in slave units [2]-[6] since they are compact and they produce high torques. However, their electric currents and metallic parts can potentially degrade the MR images [8] qualifying these components as MRI-conditional at most [9]. Conversely pneumatic and hydraulic actuation can be designed to be MRI-safe employing non-metallic materials [10]. Compared to hydraulics, pneumatic actuation is fast, clean, inexpensive and better suited for force control [11]. However, the high friction typical of pneumatic cylinders can limit the ability to provide accurate force feedback.

This work presents a master-slave system for teleoperated needle insertions in a closed bore MRI scanner (Fig. 1). Differently from previous designs [1]-[6], [8], pneumatic actuation is employed in both master and slave units in order to minimize the interference with the MRI environment. The position control of the slave unit, which is located inside the MRI scanner, is achieved with a Time Delay Control (TDC) scheme [12]. Force feedback is provided by the master unit, which sits next to the operator. In [13] pneumatic actuation was employed for bilateral teleoperation however friction forces were not compensated. Recently, a pneumatic master unit for needle insertion was presented in [2] although the force controller did not account for the friction of the pneumatic cylinder. In this work an adaptive control scheme designed using the Immersion and Invariance (I&I) method [14], [15] is employed to compensate the friction forces. Previously, an I&I adaptive controller for a pneumatic cylinder was proposed in [16], however friction was modeled as a constant force, independent of system states. The controller was extended in [17] to include stiction compensation, which however was not adaptive. The I&I method is used here to compensate nonlinear friction forces consisting of viscous friction, Coulomb friction, and stiction. Experiments on silicone rubber phantoms demonstrate the benefits of the adaptive friction compensation. The design of a simple fiber optic force sensor for the measurement of needle insertion forces in the MRI scanner is also presented.

Section II briefly describes the design of the prototype and of the fiber optic force sensor. Section III presents the adaptive force control scheme employed on the master unit. Section IV reports the experimental results and section V contains the concluding remarks.

II. System Design

The primary aim of this research is the development of a robotic assistant for the laser ablation of liver tumors under MRI-guidance [18]. The system described here represents our first step towards the teleoperated needle insertion in MRI-guided laser ablation procedures.

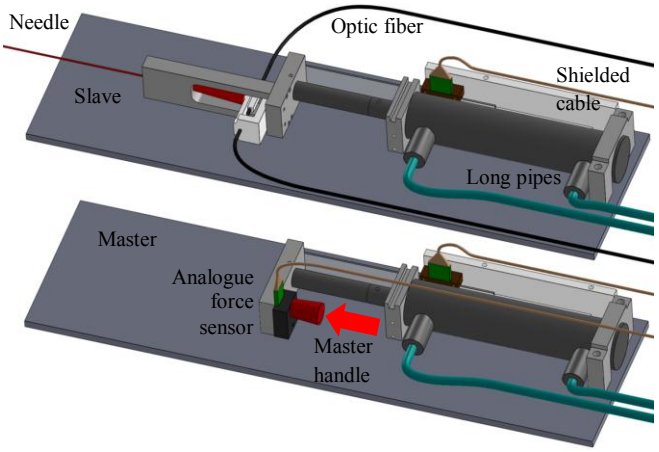


Fig. 1. CAD model of the master-slave system. The slave is located in the MRI scanner while the master sits in the MRI control room.

*Resrach supported by the i4i Grant II-AR-1109-11011.

E. Franco and M. Ristic are with the Mechanical Engineering Department, Imperial College London, SW7 2AZ, UK (e-mail: ef1311@imperial.ac.uk, m.ristic@imperial.ac.uk).

A. System Requirements

A detailed study of needle insertion forces in bovine liver and in silicone rubber phantoms was presented in [19]. Experiments showed maximum insertion forces between 4 N and 6 N for a stainless steel needle (1 mm OD, 2.65 mm/s insertion speed), while higher forces were inferred for larger needle diameters. The increase of insertion force with insertion speed in the range from 5 mm/s to 200 mm/s was reported in [20]. The increase of the insertion forces with insertion depth due to friction was highlighted in [21], which reports values in the range 1 N to 10 N. Consultations with interventional radiologists indicate that the insertion speed in laser ablation procedures is typically smaller than 10 mm/s.

B. System Design

The master-slave system has been developed for teleoperated needle insertions in closed bore MRI scanners. Plastic materials were used for the construction of the prototype since ferromagnetic components are not allowed in the MRI environment. The position of master and slave is measured with linear encoders (EMI-250, US Digital). Our previous work [12], [18] demonstrated that these sensors do not noticeably affect the quality of the MR images. Identical double-acting plastic cylinders are employed in the master and slave units (AC-111707-501, IPS Inc). The required bore size of the slave cylinder was calculated using a recursive procedure [12] and assuming a maximum insertion force of 15 N and a maximum insertion velocity of 50 mm/s. An immediately larger stock size was chosen to accommodate additional loads. Both cylinders are supplied by proportional pressure regulators (Tecno Basic, Hoerbiger) located in the control unit, outside the scanner room. The slave cylinder is connected to the proportional valves through 9 m long pipes, while the master sits next to the control unit. The proportional valves are supplied at 4 bar and control the output pressure in the range 0.3 bar to 3 bar in closed loop, using to the on-board pressure sensor. Low actuation pressure is employed in order to enhance safety and to ensure the recommended pressure drop across the valve. The CAD model of the prototype is depicted in Fig. 1.

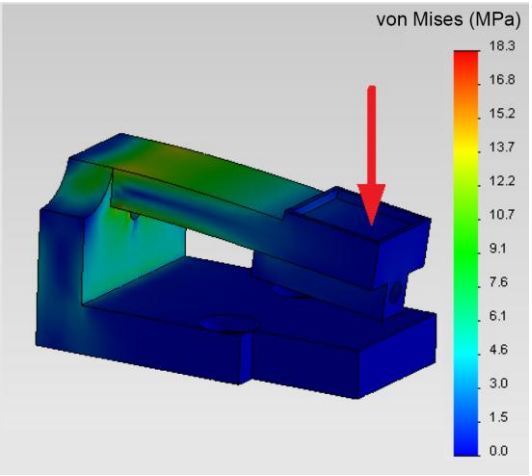


Fig. 2. Finite element analysis with 15 N vertical load (red arrow). The maximum displacement, at the tip of the cantilever, is 1.5 mm. The maximum tensile stress for ABS is in the range 30 Mpa to 50 Mpa.

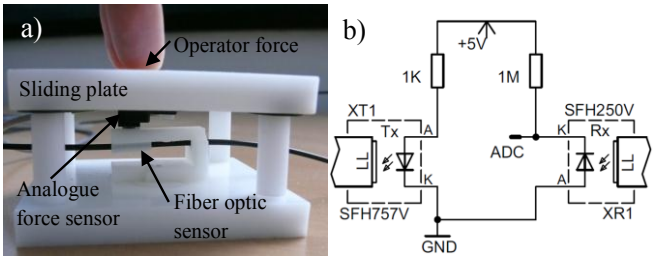


Fig. 3. Fixture used for the calibration of the fiber optic sensor (a); schematic circuit of the fiber optic sensor (b).

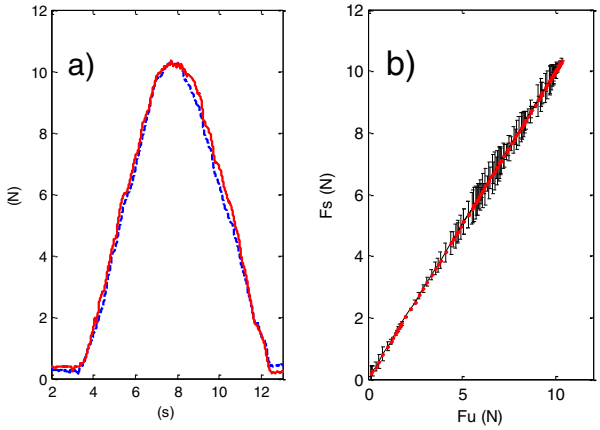


Fig. 4. Force measurements for manual compression (a): piezoresistive sensor F_u (solid red line) and fiber optic sensor F_s (dashed blue line); calibration curve of the fiber optic sensor with the piezoresistive sensor (b).

C. Fiber Optic Sensor

Fiber optic force sensors have been successfully employed in the MRI environment since they do not degrade the images and they do not interact with the magnetic field [2], [6], [8]. While good performance was achieved with different methods, previous designs rely on the accurate alignment of the optic fiber with either a reflective element or a lens, which in practice can be challenging to achieve. In this work a simple and affordable 1-DOF force sensor was developed based on the method presented in [22], which makes use of a single core fiber and does not require mirrors or lenses. The main drawback of this approach is the larger size of the sensor. Similarly to the position sensor described in [23], a segmented plastic optic fiber is used as sensitive element (413-368, RS Components, UK). Here the fiber is mounted on a cantilever structure, manufactured using a rapid prototyping material (ABS) and bends under the action of the needle force. The finite element analysis (FEA) shows that the structure can withstand the stress produced by the maximum needle force (Fig. 2). The modal analysis indicates that the first natural frequency of the structure (681 Hz) lies above the bandwidth of the pneumatic actuation, and that this vibration mode corresponds to the deflection in the vertical plane. As a consequence of the deflection, part of the light emitted by the transmitter (SFH757V, Avago Technologies, USA) at one end of the fiber escapes from the segmented fiber, and the receiver (SFH250V, Avago Technologies, USA) detects a decreasing signal. Both transmitter and receiver are located in the control unit. The receiver provides an analog signal to a 12-bit ADC therefore the

sensor resolution is better than 0.1 N. The force measurement is low-pass filterer with 10 Hz cutoff frequency. A similar range was used in [1] since it produces a smooth signal with a negligible shift in the force profile.

The fiber optic sensor was calibrated using a commercial piezoresistive force sensor (FSG15N1A, Honeywell, USA) and a specially designed fixture (Fig. 3). When a force is applied to the top plate of the fixture the load is transferred to both sensors that are in contact with each other. The linear regression of fiber optic sensor and piezoresistive sensor exhibits a coefficient of determination (R^2) of 0.99 and a maximum error of ±0.69 N (Fig. 4). In particular the measurement error limits the ability to reflect small insertion forces (ref. Section IV).

III. Controller Design

This section presents the control of the master-slave system. Part A briefly describes the control architecture of the whole system, while Part B presents the adaptive force control scheme employed in the master.

A. Control Architecture

Since pneumatic actuators are back drivable and naturally suited for force control [11] an impedance control paradigm [2] was chosen for the master-slave system (Fig. 5).

In order to perform teleoperated needle insertions the slave piston is required to accurately track the position of the master. High positioning accuracy was achieved in spite of the friction of the piston and of the delay introduced by the long supply lines with a TDC algorithm [12]. Differently from Sliding Mode Control (SMC), which is widely employed for this type of actuation [18], [24], the controller does not require previous knowledge of the maximum friction forces. Moreover it does not rely on pressure measurements in the cylinder chambers. This is beneficial since commercially available pressure sensors are typically not MRI compatible.

As part of the impedance control scheme the master unit is required to provide force feedback to the operator in real time. This information supplements the visual feedback from the intraoperative MR images, which are not available in real time. This would allow the operator to vary the insertion speed based on the resistance of the tissues, similarly to manual needle insertions.

B. Force Control

The dynamics of the master unit is modelled as:

$$A \times P_1 - A' \times P_2 + F_u = m\ddot{x} + \gamma \dot{x} + F_a \operatorname{sign}(\dot{x}) \qquad \dot{x} \neq 0 \qquad (1a)$$

$$A \times P_1 - A' \times P_2 + F_u = m\ddot{x} + F_m \qquad \dot{x} = 0 \qquad (1b)$$

The terms A, A', m are respectively the effective piston areas and the mass of piston and payload. The terms P_1 and P_2 are the controlled pressures in the back and in the front cylinder chambers. The terms γ, F_a, F_m are the unknown values of viscous friction, Coulomb friction and stiction while the term F_u is the operator force. The piston position x is measured with the linear encoder while the velocity $\dot{x}$ is calculated by discrete differentiation and low pass filtering (50 Hz cutoff frequency). Similarly to [24] the much faster dynamics of the proportional valves (bandwidth > 100 Hz) is not considered in the design. Since the master sits next to the control unit the effect of the pipes is assumed negligible and is disregarded. Consequently, P_1 and P_2 are considered equal to the output pressures of the proportional valves, which are controlled in closed loop by the on-board PID. The control objective for the master is to produce a force on the operator equal to the insertion force F_s that is measured on the slave:

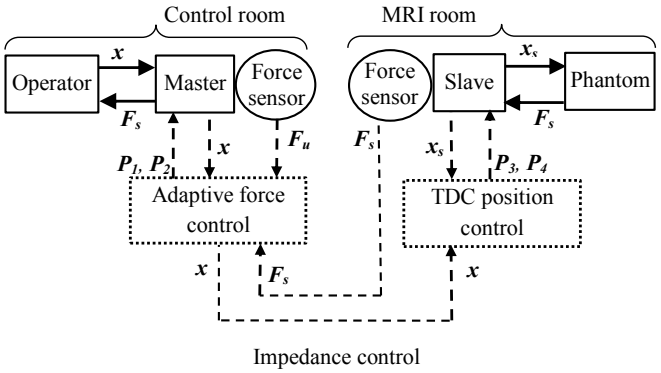


Fig. 5. Control architecture of the master-slave system: solid lines represent physical interactions; dashed lines represent signals.

$$F_u = F_s \qquad (2)$$

Assuming negligible friction and inertial forces this goal can be achieved with the baseline control law [2]:

$$P_1 = \left(A' \times P_2 - F_s\right) / A \qquad (3)$$

where P_2 is set constant here for simplicity. Neglecting the inertial forces appears plausible for a small mass m and for slow movements. However, while needle insertion forces are generally small (ref. Section II), commercial cylinders typically have high friction [12]. Consequently, disregarding friction could drastically degrade the performance of the controller and devaluate the force feedback on the operator (ref. Section IV). While magnifying the insertion forces would improve the operator's perception, the measurement noise would also be amplified causing unwanted vibrations. These could be reduced with more aggressive filtering that however would introduce a noticeable phase shift.

Friction forces are typically difficult to estimate with sufficient accuracy and their magnitude can slowly vary due to wear and working conditions. An adaptive control scheme is employed here to compensate viscous friction, Coulomb friction, and stiction in (1a), (1b). The Immersion and Invariance (I&I) method [14], [15] was chosen because of its modularity, which makes it suitable for different control schemes. Additionally, the resulting controller contains a limited number of parameters, which simplifies tuning. In particular, a single parameter is sufficient here to estimate both viscous friction and Coulomb friction, while a second parameter is required for the estimate of the stiction.

The design of the adaptive controller is split into two cases corresponding to equations (1a) and (1b).

Case 1: $\dot{x} \neq 0$. We start considering equation (1a) which for notational convenience is rewritten as:

$$\begin{cases} \dot{x}_1 = x_2 \\ \dot{x}_2 = \left(A \times P_1 - A' \times P_2 + F_u - \gamma x_2 - F_a \operatorname{sign}(x_2)\right) / m \end{cases} \qquad (4)$$

We then define the estimation errors z_1 and z_2 for both terms γ and F_a which are assumed independent of the system states:

$$z_1 = \hat{\gamma} + \beta_1 - \gamma \tag{5a}$$

$$z_2 = \hat{F}_a + \beta_2 - F_a \tag{5b}$$

The nonlinear functions β_1, β_2, $\hat{\gamma}$, $\hat{F}_a$ are defined in the following steps in order to ensure convergence of the estimation errors to zero. For this purpose a positive definite Lyapunov candidate function is chosen as:

$$V_1 = z_1^2 + z_2^2 \tag{6}$$

The estimation errors z_1 and z_2 will converge to zero if the adaptation law makes the Lyapunov function derivative negative definite:

$$\dot{V}_1 = z_1 \dot{z}_1 + z_2 \dot{z}_2 < 0 \tag{7}$$

Differentiating (5a), (5b) and substituting (4) we obtain:

$$\begin{aligned} \dot{z}_1 = {} & \dot{\hat{\gamma}} + \frac{\partial \beta_1}{\partial x_1} x_2 + \frac{\partial \beta_1}{\partial x_2} \left(A \times P_1 - A' \times P_2 + F_u \right) / m + \\ & - \frac{\partial \beta_1}{\partial x_2} \left(\left(\hat{\gamma} + \beta_1 - z_1 \right) x_2 + \left(\hat{F}_a + \beta_2 - z_2 \right) \operatorname{sign}(x_2) \right) / m \end{aligned} \tag{8a}$$

$$\begin{aligned} \dot{z}_2 = {} & \dot{\hat{F}}_a + \frac{\partial \beta_2}{\partial x_1} x_2 + \frac{\partial \beta_2}{\partial x_2} \left(A \times P_1 - A' \times P_2 + F_u \right) / m + \\ & - \frac{\partial \beta_2}{\partial x_2} \left(\left(\hat{\gamma} + \beta_1 - z_1 \right) x_2 + \left(\hat{F}_a + \beta_2 - z_2 \right) \operatorname{sign}(x_2) \right) / m \end{aligned} \tag{8b}$$

At this point we postulate that with an appropriate choice of $\dot{\hat{\gamma}}$ and $\dot{\hat{F}}_a$ the error dynamics becomes:

$$\dot{z}_1 = \frac{\partial \beta_1}{\partial x_2} \left(z_1 x_2 + z_2 \operatorname{sign}(x_2) \right) / m \tag{9a}$$

$$\dot{z}_2 = \frac{\partial \beta_2}{\partial x_2} \left(z_1 x_2 + z_2 \operatorname{sign}(x_2) \right) / m \tag{9b}$$

Taking advantage of the structure of (9a), (9b) the update laws for the functions β_1 and β_2 are chosen as:

$$\frac{\partial \beta_1}{\partial x_2} = -\alpha_1 x_2 m \tag{10a}$$

$$\frac{\partial \beta_2}{\partial x_2} = -\alpha_1 \operatorname{sign}(x_2) m \tag{10b}$$

where α_1 is a positive tuning parameter. Substituting (10a), (10b) and (9a), (9b) into (7) the convergence is proved:

$$\dot{V}_1 = -\alpha_1 \left(z_1^2 x_2^2 + z_2^2 + 2 z_1 z_2 |x_2| \right) = -\alpha_1 \left(z_1 |x_2| + z_2 \right)^2 \tag{11}$$

Finally, the complete formulation of the adaptation law is obtained integrating (10a), (10b) and choosing $\dot{\hat{\gamma}}$ and $\dot{\hat{F}}_a$ in (8a), (8b) so that (9a), (9b) are verified:

$$\begin{aligned} \dot{\hat{\gamma}} = {} & \alpha_1 x_2 \left(A \times P_1 - A' \times P_2 + F_u \right) + \\ & - \alpha_1 x_2 \left(\left(\hat{\gamma} + \beta_1 \right) x_2 + \left(\hat{F}_a + \beta_2 \right) \operatorname{sign}(x_2) \right) \end{aligned} \tag{12a}$$

$$\begin{aligned} \dot{\hat{F}}_a = {} & \alpha_1 \operatorname{sign}(x_2) \left(A \times P_1 - A' \times P_2 + F_u \right) + \\ & - \alpha_1 \operatorname{sign}(x_2) \left(\left(\hat{\gamma} + \beta_1 \right) x_2 + \left(\hat{F}_a + \beta_2 \right) \operatorname{sign}(x_2) \right) \end{aligned} \tag{12b}$$

$$\beta_1 = -\alpha_1 m x_2^2 / 2 \tag{12c}$$

$$\beta_2 = -\alpha_1 m |x_2| \tag{12d}$$

The control law for the case $x_2 \neq 0$ is:

$$P_1 = \left(A' \times P_2 + \left(\hat{\gamma} + \beta_1 \right) x_2 + \left(\hat{F}_a + \beta_2 \right) \operatorname{sign}(x_2) - F_s \right) / A \tag{13}$$

It must be noted that the piston velocity x_2 appears as a multiplier in the adaptation law (12a)-(12d) whose structure is consequently not appropriate to compensate stiction.

Case 2: $\dot{x} = 0$. We consider now the equation (1b) which is rewritten as:

$$\begin{cases} \dot{x}_1 = x_2 \\ \dot{x}_2 = \left(A \times P_1 - A' \times P_2 + F_u - F_m \right) / m \end{cases} \tag{14}$$

We define the estimation error z_3 for the term F_m which is assumed independent of the system states:

$$z_3 = \hat{F}_m + \beta_3 - F_m \tag{15}$$

where the nonlinear functions β_3, and $\hat{F}_m$ are defined in the following steps. To ensure convergence of z_3 a positive definite Lyapunov function and its derivative are defined as:

$$V_2 = z_3^2 \tag{16}$$

$$\dot{V}_2 = z_3 \dot{z}_3 < 0 \tag{17}$$

Differentiating (15) and substituting (14) we obtain:

$$\begin{aligned} \dot{z}_3 = {} & \dot{\hat{F}}_m + \frac{\partial \beta_3}{\partial x_1} x_2 + \frac{\partial \beta_3}{\partial x_2} \left(A \times P_1 - A' \times P_2 + F_u \right) / m + \\ & - \frac{\partial \beta_3}{\partial x_2} \left(\left(\hat{F}_m + \beta_3 - z_3 \right) \right) / m \end{aligned} \tag{18}$$

We assume that an appropriate choice of $\dot{\hat{F}}_m$ can result in the following error dynamics:

$$\dot{z}_3 = \frac{\partial \beta_3}{\partial x_2} \frac{z_3}{m} \tag{19}$$

The update law for the functions β_3 is then chosen as:

$$\frac{\partial \beta_3}{\partial x_2} = -\alpha_2 m \tag{20}$$

where α_2 is a positive tuning parameter. Substituting (20) and (19) in (17) the convergence is proved:

$$\dot{V}_2 = -\alpha_2 z_3^{\,2} < 0 \tag{21}$$

The adaptation law is obtained integrating (20) and choosing $\dot{\hat{F}}_m$ in (18) so that (19) is verified:

$$\beta_3 = -\alpha_2 m x_2 \tag{22a}$$

$$\dot{\hat{F}}_m = \alpha_2 \left(A \times P_1 - A' \times P_2 + F_u - \left(\hat{F}_m + \beta_3 \right) \right) \tag{22b}$$

The control law for the case $x_2 = 0$ is:

$$P_1 = \left(A' \times P_2 + \left(\hat{F}_m + \beta_3 \right) - F_s \right) / A \tag{23}$$

From $x_2 = 0$ follows that $\beta_3 = 0$, hence it can be easily verified that the adaptation law (22a), (22b) is in fact an integrator with input $(F_u - F_s)$.

IV. Experimental Results

Experimental tests on silicone rubber phantoms were conducted to evaluate the performance of the master-slave system. This study is limited to positive insertion forces and particular attention is paid to the relation between operator force and insertion force.

A. Test Setup

The needle insertion tests were performed on three different silicone rubber phantoms (Table I). A 14G coaxial needle (1.2 mm OD) was mounted on the slave unit in contact with the fiber optic force sensor (Fig. 6). A commercial force sensor (FSG15N1A, Honeywell, USA) was employed on the master unit (Fig. 1). The operator applied a force F_u on the master moving the piston to the desired position. The insertion force F_s measured on the slave was reflected on the master by the control. In the tests no visual feedback of the slave was provided.

Both the baseline force control (3) and the adaptive control scheme (13)-(23) were programmed on a microcontroller (mbed NHP LPC1768) at 1.5 kHz sampling frequency. The TDC scheme [12] was employed for the position control of the slave. The system and controller parameters, which were manually tuned, are listed in Table II. The controlled pressures in master and slave were limited in the range 0.3 bar to 3 bar (ref. Section II). Additionally a dead band was introduced in the force controllers so that the force feedback is activated only if the operator force F_u is larger than a positive threshold. This approach is motivated considering that the insertion force F_s is only reactive and as such it should not cause a movement of the master against the operator. In practice this might occur as a result of measurement errors and noise in the force sensors. Hence, the threshold was set higher than the maximum error of the fiber optic sensor.

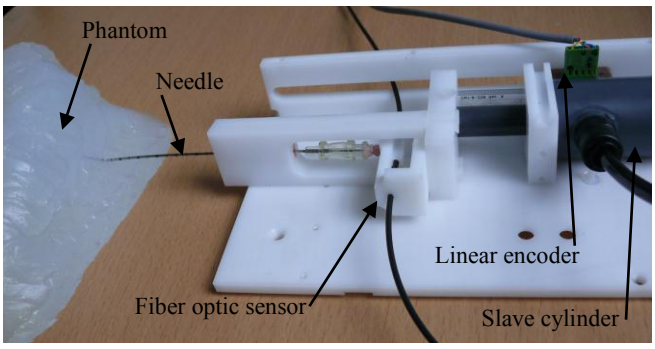


Fig. 6. Test setup for the slave unit. Both phantom and slave cylinder are secured to the desk with clamps. The master unit sits next to the operator.

TABLE I
PHANTOM PROPERTIES

Phantom	Volume (dm^3)	Mass (Kg)	Density (Kg/dm^3)	Distance from the slave (mm)
A	0.45	0.45	1.00	20
B	0.45	0.39	0.87	20
C	0.39	0.20	0.51	65

TABLE II
SYSTEM AND CONTROLLER PARAMETERS

Parameters	m	A	A'	P_2	α_1	α_2
Value	0.1	285	158	3.0	2	10
Unit	Kg	mm^2	mm^2	bar	-	-

B. Results and Discussion

For each phantom both the baseline and the adaptive force control schemes were tested on the master. In each test the position of master and slave, the needle insertion force

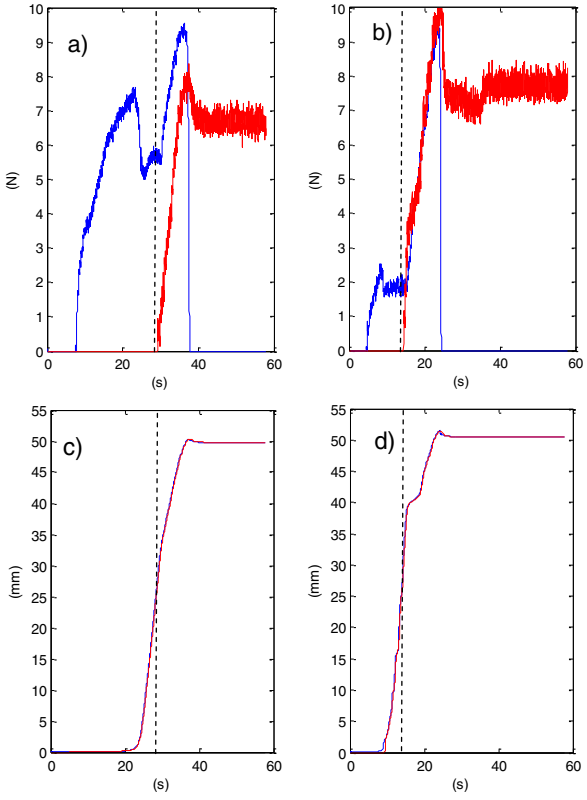


Fig. 7. Needle insertion on phantom A: forces (a) and positions (c) for the baseline controller (3); forces (b) and positions (d) for the adaptive controller (13)-(23). Master position x and operator force F_u are plotted in blue; slave position x_s and needle force F_s are plotted in red.

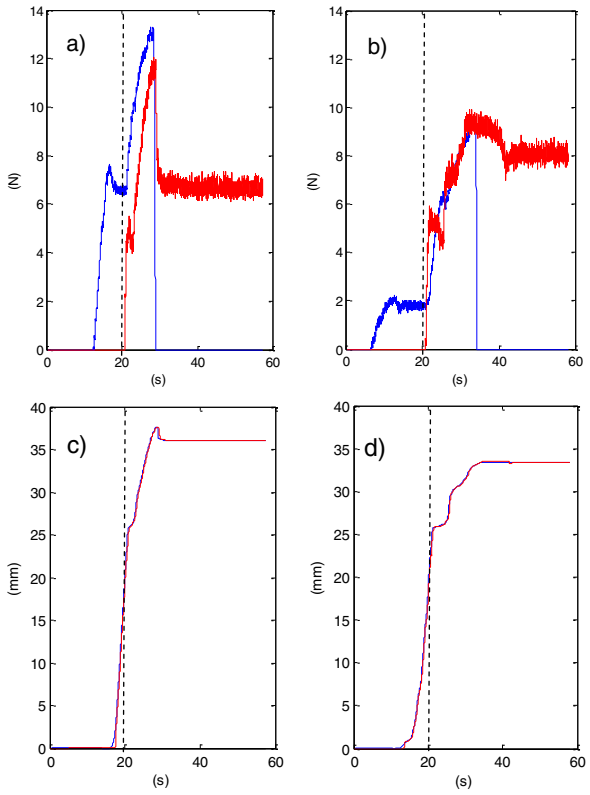


Fig. 8. Needle insertion on phantom B: forces (a) and positions (c) for the baseline controller (3); forces (b) and positions (d) for the adaptive controller (13)-(23); Master position x and operator force F_u are plotted in blue; slave position x_s and needle force F_s are plotted in red.

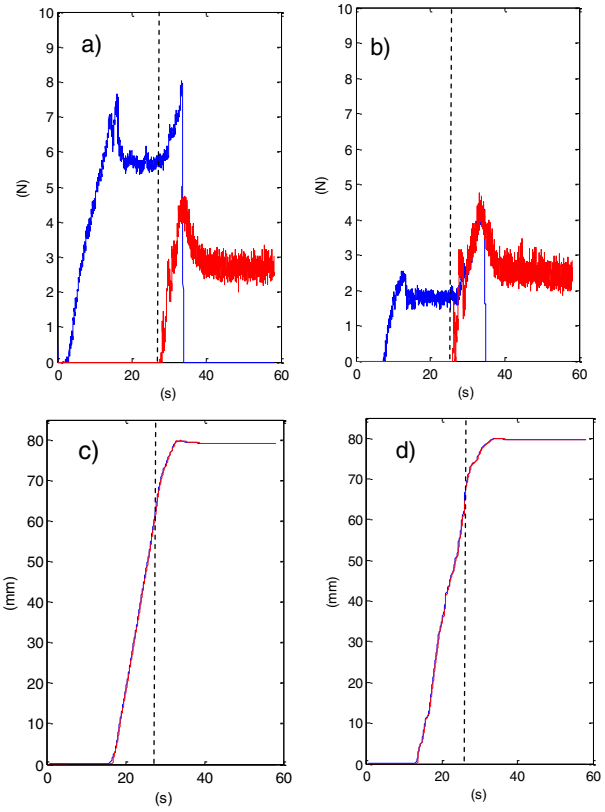


Fig. 9. Needle insertion on phantom C: forces (a) and positions (c) for the baseline controller (3); forces (b) and positions (d) for the adaptive controller (13)-(23); Master position x and operator force F_u are plotted in blue; slave position x_s and needle force F_s are plotted in red.

and the operator force were recorded. The results of the tests on phantom A are depicted in Fig. 7. The initial contact with the phantom is represented by a dashed vertical line. It is apparent that with the adaptive controller the operator can move the master piston using a smaller force compared to the baseline scheme. In particular, the adaptive algorithm compensates viscous and Coulomb friction as well as stiction. It must be noted however that, due to the dead band introduced in the controllers, a minimum force is still required to move the master. Above this value the operator force F_u follows closely the insertion force F_s. The discrepancy between F_u and F_s for $F_u > 0$ is measured with the root-mean-square-error (RMSE) reported in Table III. The adaptive force controller results in a smaller RMSE for all test conditions, implying better transparency. The position plots indicate that the operator instinctively reacts reducing the insertion speed after detecting the puncture. This effect is more noticeable with the adaptive force controller suggesting a clearer detection and it can be explained considering that human sensing resolution depends on the force intensity [25]. Since with the adaptive controller a smaller effort is required to move the master piston, the operator's ability to detect a force variation is enhanced. Similar results are shown for phantom B in Fig. 8. In this case the force profile shows rapid oscillations as the insertion progresses. A similar behavior was observed in [19] and could be related to the internal inhomogeneity of this phantom. The results for phantom C are depicted in Fig. 9. Since this phantom has a lower density compared to the other two, the insertion force is smaller and increases more gradually with the insertion depth. As a result the movement of master and slave is more uniform however detecting the puncture using the force feedback is more difficult. In this case the adaptive force controller proves most useful: both the operator force and the master position show a clearer change in their trend at about 30 s indicating that the needle has punctured the phantom.

Maximum tracking error and RMSE for the slave cylinder are listed in Table IV. The values are comparable to those reported in [12], which were obtained for a different cylinder and payload. The results are similar for both force controllers and indicate that this choice does not affect the tracking accuracy of the slave. The maximum error remains

TABLE III
FORCE TRACKING OF THE MASTER

Controller	Baseline controller (3)			Adaptive controller (13)-(23)		
Phantom	A	B	C	A	B	C
RMSE (N)	3.90	2.73	3.80	0.92	1.09	1.08

TABLE IV
POSITION TRACKING OF THE SLAVE

Controller	Baseline controller (3)			Adaptive controller (13)-(23)		
Phantom	A	B	C	A	B	C
Maximum error (mm)	1.32	2.97	1.65	2.49	1.32	2.54
RMSE (mm)	0.28	0.35	0.39	0.41	0.25	0.41

below 5 mm which corresponds to the radius of the smallest lesions normally treated with the laser ablation procedure [26], suggesting that the positioning accuracy of the system is appropriate for the application.

V. Conclusion

In this paper the control of a master-slave unit for MRI-guided needle insertion is presented. The system employs pneumatic actuation in both master and slave units and includes a simple fiber optic sensor for the measurement of needle insertion forces. An adaptive force controller is employed to compensate the friction forces on the master and to reflect the needle force on the operator. Experiments with silicone rubber phantoms confirm that the adaptive controller reduces the operator's effort, improves the transparency of the system, and results in easier detection of the puncture compared to a baseline control algorithm. Further work will include validation of the system in the MRI scanner and tests with different operators. Finally the master-slave system will be integrated into a needle-guiding robot for MRI-guided laser ablation of liver tumors.

Acknowledgment

The Authors wish to thank Alessandro Astolfi for the several stimulating discussions on control theory, and Alessandro Allievi for sharing his knowledge of fiber optic sensors.

References

[1] Kokes, R.; Lister, K.; Gullapalli, R.; Zhang, B.; MacMillan, A.; Richard, H.; Desai, J., "Towards a teleoperated needle driver robot with haptic feedback for RFA of breast tumors under continuous MRI," *Medical Image Analysis*, vol. 13, no. 3, pp. 445-455, 2009.

[2] Weijian Shang; Hao Su; Gang Li; Fischer, G.S., "Teleoperation system with hybrid pneumatic-piezoelectric actuation for MRI-guided needle insertion with haptic feedback," *Proceedings of the IEEE/RSJ International Conference on Intelligent Robots and Systems (IROS),* pp.4092,4098, 3-7 Nov. 2013.

[3] Seifabadi, R.; Song, S. E.; Krieger, A.; Cho, N. B.; Tokuda, J.; Fichtinger, G.; Iordachita I., "Robotic system for MRI-guided prostate biopsy: Feasibility of teleoperated needle insertion and ex vivo phantom study," *Int. J. Comput. Assist. Radiol. Surg*., vol. 7, no. 2, pp. 181–190, 2012.

[4] Seifabadi, R.; Iordachita, I.; Fichtinger, G., "Design of a teleoperated needle steering system for MRI-guided prostate interventions," *Proceedings of the IEEE RAS and EMBS International Conference on Biomedical Robotics and Biomechatronics,* pp. 793–798, 2012.

[5] Tse, Z.; Elhawary, H.; Rea, M.; Davies, B.; Young, I.; Lamperth, M., "Haptic Needle Unit for MR-Guided Biopsy and Its Control," *Mechatronics, IEEE/ASME Transactions on*, vol. 17, pp. 183 –187, Feb. 2012.

[6] Su, H.; Zervas, M.; Cole, G.; Furlong, C.; Fischer, G. S., "Realtime MRI-Guided Needle Placement Robot with Integrated Fiber Optic Force Sensing," *Proceedings of the IEEE International Conference on Robotics and Automation (ICRA),* pp. 1583–1588, 2011.

[7] Elhawary, H.; Tse, Z, T.; Hamed, A.; Rea, M.; Davies, B., L.; Lamperth, M., U., "The case for MR-compatible robotics: a review of the state of the art," *Int J Med Robot*, 2008. vol. 4, no. 2, pp. 105–113.

[8] Bo Yang; U-Xuan Tan; McMillan, A.; Gullapalli, R.; Desai, J.P., "Design and implementation of a pneumatically-actuated robot for breast biopsy under continuous MRI," *Proceedings of IEEE the International Conference on Robotics and Automation (ICRA),* pp.674-679, 9-13 May 2011.

[9] ASTM International Standard, "ASTM F2503-13, *Standard Practice for Making Medical Devices and Other Items for Safety in the Magnetic Resonance Environment*," 06/01/2013.

[10] Stoianovici, D.; Chunwoo Kim; Srimathveeravalli, G.; Sebrecht, P.; Petrisor, D.; Coleman, J.; Solomon, S.B.; Hricak, H., "MRI-Safe Robot for Endorectal Prostate Biopsy," *Mechatronics, IEEE/ASME Transactions on* , vol.19, no.4 , pp.1289,1299, Aug. 2014.

[11] Yu N.; Hollnagel, C.; Blickenstorfer, A.; Kollias, S.; Riener, R., "Comparison of MRI-Compatible Mechatronic Systems With Hydrodynamic and Pneumatic Actuation," *Mechatronics, IEEE/ASME Transactions on*, vol. 13, pp. 268 –277, june 2008.

[12] Franco, E.; Ristic, M., "Time Delay Controller for the Position Control of a MRI-compatible Pneumatic Actuation with Long Supply Lines," *Proceedings of the IEEE/ASME International Conference on Advanced Intelligent Mechatronics (AIM)*, pp.683-689, 8-11 Jul. 2014.

[13] Durbha, V.; Li, P. Y., "Passive Bilateral Tele-Operation and Human Power Amplification with Pneumatic Actuators," *Proceedings of the ASME Dynamic Systems and Control Conference*, 2009, pp.863-870.

[14] Astolfi, A.; Ortega, R., "Immersion and Invariance: A New Tool for Stabilization and Adaptive Control of Nonlinear Systems," *IEEE Transactions on Automatic Control*, vol. 48, no. 4, pp. 590-606, 2003.

[15] Astolfi A.; Karagiannis D.; Ortega R., *Nonlinear and adaptive control with applications*, Springer-Verlag, Berlin, 2007.

[16] Rapp, P.; Klunder, M.; Sawodny, O.; Tarin, C., "Nonlinear adaptive and tracking control of a pneumatic actuator via immersion and invariance," *Proceedings of the IEEE 51st Annual Conference on Decision and Control (CDC)*, pp.4145-4151, 10-13 Dec. 2012.

[17] Pradipta, J.; Klunder, M.; Weickgenannt, M.; Sawodny, O., "Development of a pneumatically driven flight simulator Stewart platform using motion and force control," *Proceedings of the IEEE/ASME International Conference on Advanced Intelligent Mechatronics (AIM)*, pp.158-163, 9-12 July 2013.

[18] Franco, E.; Ristic, M., "Design and Control of Needle Positioner for MRI-guided Laser Ablation of the Liver," *Proceedings of the IEEE/ASME International Conference on Mechatronics and Embedded Systems and Applications (MESA)*, pp.1-6, 10-12 Sep. 2014.

[19] Okamura, A.M.; Simone, C.; O'Leary, M.D., "Force modeling for needle insertion into soft tissue," *Biomedical Engineering, IEEE Transactions on*, vol.51, no.10, pp.1707, 1716, Oct. 2004.

[20] Podder, T.K.; Clark, D.P.; Fuller, D.; Sherman, J.; Ng, W.S.; Liao, L.; Rubens, D.J.; Strang, J.G.; Messing, E.M.; Zhang, Y.D.; Yu, Y., "Effects of Velocity Modulation during Surgical Needle Insertion," *Proceedings of the IEEE-EMBS 27th Annual International Conference of the Engineering in Medicine and Biology Society*, pp.5766-5770, 2005

[21] van Gerwen, Dennis J.; Dankelman, Jenny; van den Dobbelsteen, John J., "Needle–tissue interaction forces – A survey of experimental data," *Medical Engineering & Physics*, Volume 34, Issue 6, Pages 665-680, July 2012.

[22] Kuang, K. S. C.; Cantwell, W. J.; Scully, P. J., "An evaluation of a novel plastic optical fibre sensor for axial strain and bend measurements," *Measurement Science and Technology,* vol. 13, no. 10. pp. 1523–1534, 2002.

[23] Allievi, A., G.; Mendelez-Calderon, A.; Arichi, T.; Edwards, A., D.; Burdet, E. "An fMRI Compatible Wrist Robotic Interface to Study Brain Development in Neonates," *Annals of Biomedical Engineering*, June 2013, Vol. 41, Issue 6, pp 1181-1192.

[24] Bo Yang; U-Xuan Tan; McMillan, A.B.; Gullapalli, R.; Desai, J.P., "Design and Control of a 1-DOF MRI-Compatible Pneumatically Actuated Robot With Long Transmission Lines," *Mechatronics, IEEE/ASME Transactions on* , vol.16, no.6, pp.1040,1048, Dec. 2011

[25] Tan, Hong Z.; Srinivasan, Mandayam A.; Eberman, Brian; Cheng, Belida, "Human factors for the design of force-reflecting haptic interfaces," *Dynamic Systems and Control*, DSC–Vol.55–1, pages 353–359,1994.

[26] Gough-Palmer, A.L.; Gedroyc, W.M. "Laser ablation of hepatocellular carcinoma--a review," *World J Gastroenterol.* 2008.